Nominal Capacity	1 Ah
Charge Cut-Off Voltage	4.2 V
Discharge Cut-Off Voltage	3.0 V
PE Material	NMC622 (poly crystal)
PE Active Material Ratio	96.4 %
PE Binder	PVDF
PE press density	3.3 g/cm³
PE Porosity	31.3 %
PE Area	519.12 cm²
PE Areal Cap.	2.24 mAh/cm²
PE Coating Thickness	42.5 μm
PE Number of sheets	12
NE Material	Artificial Graphite
NE active material ratio	95.7 %
NE Binder	CMC+SBR
NE press density	1.5 g/cm³
NE Porosity	31.8 %
NE Area	637.65 cm²
NE Areal Cap.	2.24 mAh/cm²
NE Coating Thickness	50 μm
NE Number of sheets	13

Table S1 Cell properties as obtained from the manufacturer's datasheet.

Supporting Information

Cell Properties

Table S1 contains the cell design parameters obtained from the manufacturer.

Discussion of Errors during Capacity Measurements

Capacity measurements, like all measurements are influenced by inaccuracies and errors. Here we provide background, on how the range was calculated.

First of all, the measured capacity is influenced not only by the actual capacity but also by a premature or delayed end of charge caused by errors in voltage or current measurements (ε_{EOC}), by a similar error affecting the end of discharge (ε_{EOC}), and the integration of the current error during discharging ($\int \varepsilon_{current} dt$). Equation 3 gives a mathematical expression for this.

$$\kappa_{measured} = \kappa_{true} + \varepsilon_{EOC} + \int \varepsilon_{current} dt + \varepsilon_{EOD} \tag{3}$$

For errors resulting in a decrease of the measured capacity compared to the true value we considered a premature stop of the charging process, an underestimation of the current during discharge and a premature stop of the discharging process. The hypothetical additional charge during the CV-phase of the charging process is estimated by fitting the exponential decay function given in Equation 4 for the current relaxation and assuming a constant offset of ε_I. The error induced by the voltage is calculated based on incremental capacity ($\frac{dQ}{dV}$) in the voltage range between 4.1 and 4.2 V during the C/20 qOCV charge.

$$I(t) = I_0 + c \cdot e^{\frac{-tau}{t}} \tag{4}$$

During discharge the maximum current error is multiplied with the time of the discharge step this approximates the error due to the integration of a faulty current. This contribution is the largest of the three error types. It is smaller, if the mean of the error is lower than the maximum error calculated based on the accuracy from the datasheet of the cycler. The error caused by a premature end of discharge is calculated based on the mean incremental capacity ($\frac{dQ}{dV}$) in the voltage range from 3 to 3.1 V. This value is multiplied by the voltage error ε_V. The maximum positive capacity error is the sum of these individual errors.

Positive errors, causing an overestimation of the capacity, require a slightly different approach. Assuming that the true voltage is shifted by ε_V, the additional charge during the CC-phase is the difference between the Ah-counting at the end of the CC-phase and the point where $V_{measured} = V_{cc,max} - \varepsilon_V$. The analogue approach is used to obtain the difference caused by an overestimation of the current during the CV-phase and an overestimation of the cell voltage during discharge. For the current error the same approach as described above is used.

The accuracy of the Neware devices used in this work is given as 0.05 % of the full scale for both current and voltage. Two different current ranges are used. One covers small currents up to 100 mA, and is relevant for the qOCV-measurements. The second range, relevant for all other capacity measurements covers current up to 6 A. The maximum voltage is 5 V. This results in a worst case error in the range of $\pm$14 mAh for the C/2 capacity measurement. The lower current range in the qOCV-measurements results in a lower error in the range of $\pm$ 2.5 mAh. Unfortunately no information on the precision of the device is provided. The accuracy of the Maccor device used for formation is given as $\pm$0.02 % of the full scale. Due to the longer duration of the formation cycle, the resulting error on the capacity charged during the first cycle remains in the same range as for the Neware systems ($\pm$14 mA).

Reference Performance Test

The reference performance test consists of an initial discharge, followed by a C/2 capacity check (CC-CV-Charge, CC Discharge), a C/20 qOCV cycle, and pulse tests with 1 C and C/2 in charge and discharge direction for 15 s at 0 and 50% SOC (based on the capacity check). The procedure is displayed in Figure S1.

Thermal Electrolyte Analysis

Here we will derive the mathematical terms used for the TEA.

During TEA experiments the temperature on the outer surface of the styrofoam block, referred to as $T_{ambient}$ and the temperature on the surface of the cell, referred to as T_{cell} is recorded. For reasons of redundancy, we applied two sensors on each side of the cell and two sensors on different sides of the polystyrene foam cubes. We use the mean of the two sensors on the cell as T_{cell} and the mean of the two sensors on the polystyrene foam cubes as $T_{ambient}$.

We will now derive a term proportional to the heat flow which can be calculated based on the measured temperatures. Assuming conductive heat transfer from ambient air through the polystyrene foam to the cell, the temperature difference ΔT as defined in Equation 5 is the driving force of the heat flow.

$$\Delta T = T_{Ambient} - T_{Cell} \tag{5}$$

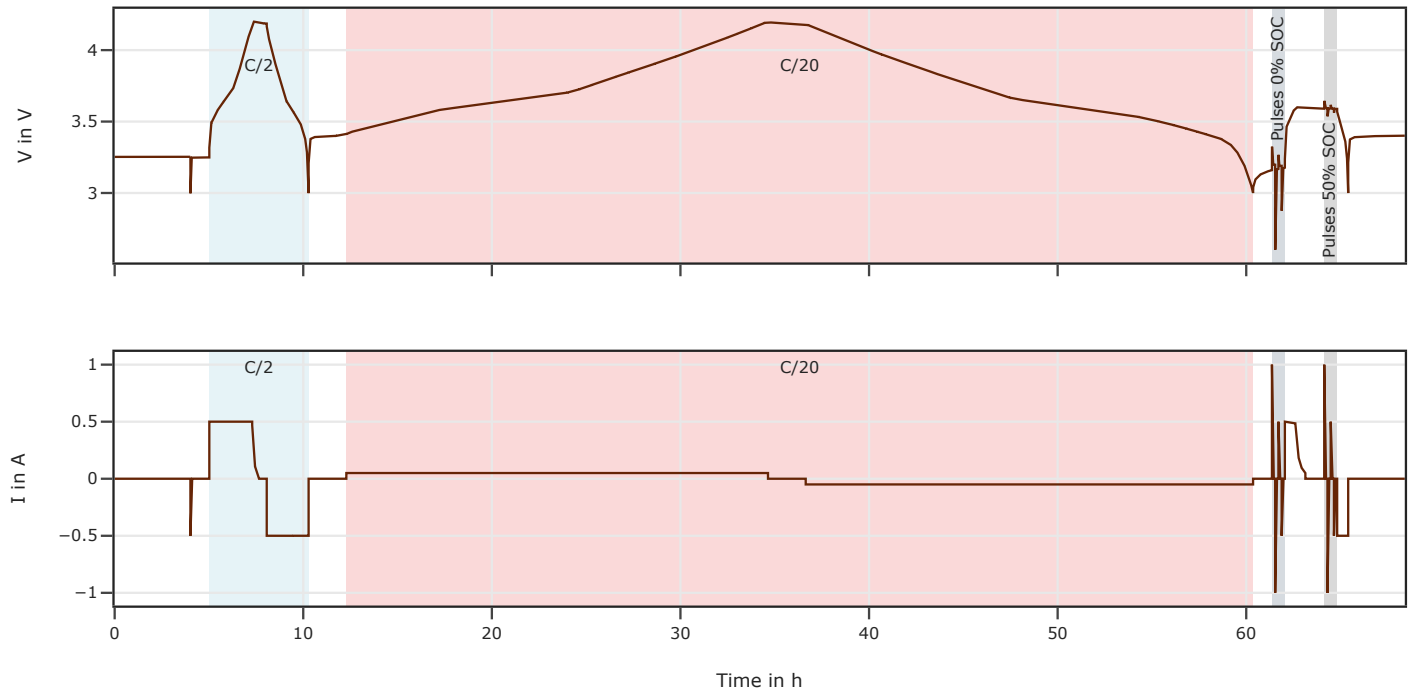

Fig. S1 Exemplary current and voltage during the RPT.

$$\dot{Q}_{cond.} = \frac{\Delta T}{R_{th}} \tag{6}$$

Conductive heat transfer can be described by Equation 6 with a thermal resistor R_{th}. The transferred energy will increase the temperature of the cell, if there is no phase change. This results in Equation 7.

$$\dot{Q}_{cond.} = \frac{dT_{cell}}{dt} \cdot C \tag{7}$$

A phase change (e.g. melting of the electrolyte) diverts energy from the heating of the cell to the phase transition. Thus, giving Equation 8

$$\dot{Q}_{cond.} - \dot{Q}_{Melting} = \frac{dT_{cell}}{dt} \cdot C \tag{8}$$

By inserting Equation 6 in Equation 8, and separating the variables that can be obtained from a single measurement ($\Delta T(t)$ and $T_{cell}(t)$) we get Equation 9

$$\frac{\Delta T(t)}{\frac{dT_{cell}(t)}{dt}} = R_{th} \cdot C + R_{th} \cdot \frac{\dot{Q}_{Melting}}{\frac{dT_{cell}(t)}{dt}} \tag{9}$$

Together with Equation 10 this results in Equation 11 which represents the required energy as a function of the temperature. To quantify the results reference measurements with materials with a known heat capacity or melting enthalpy can be used to calculate R_{th}. Division of Equation 11 by R_{th} and integration between two temperatures will yield the required energy to heat the device under test (a battery cell, or another object used for calibration) between these temperatures. A baseline correction can be performed with a dry cell, containing no electrolyte.

$$\dot{Q}_{Melting} = \frac{dQ_{Melting}}{dt} \tag{10}$$

$$\frac{\Delta T}{\frac{dT_{cell}}{dt}} = R_{th} \cdot C + R_{th} \cdot \frac{dQ_{Melting}}{dT_{cell}} \tag{11}$$

DSC measurements

The calibration of the DSC was performed using the same technique and polynomial functions described in the previous publication[50], but using the following calibration substances to cover the temperature range used in this work: cyclohexane, adamantane ($C_{10}H_{16}$), water and indium. For cyclohexane both phase transition (solid-solid phase transition at -88.6 °C and the solid-liquid transition at 7.2 °C) were used for the calibration. The calibration leads to a temperature accuracy of ± 1 °C for the temperatures measured by DSC according to Hoehne et al.[51].

The melting behaviour of the electrolyte was first described by Ding et al[52] and is in good agreement with our measurements, as the used electrolyte composition is comparable. In the following the melting behaviour of the electrolyte containing crystallisation nuclei, in our case sheets of separator, is described based on the work of Ding et al. During the cooling ramp of the experiment the viscosity of the electrolyte becomes so high, that there only slight crystallisation of the electrolyte occures, which leads to a glass transition. The glass transition occurs again in the heating mode, which is visible in Figure S2 at around -120 °C. This is followed by an exothermic peak, highest at -93 °C, which indicates the crystallisation of the rest of the electrolyte, due to the now possible diffusion. The eutectic temperature is indicated by the endothermic peak, highest at -60 °C, followed by the melting of the electrolyte until the liquidus temperature at -34 °C is reached.

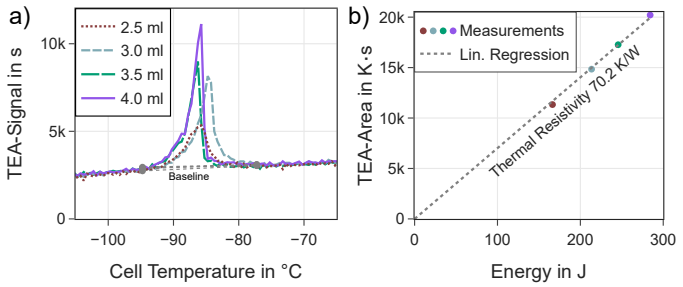

Fig. S3 a) TEA-measurement of the melting process of different amounts of 2-propanol. b) the linear regression used to calculate the thermal conductivity of the styrofoam blocks

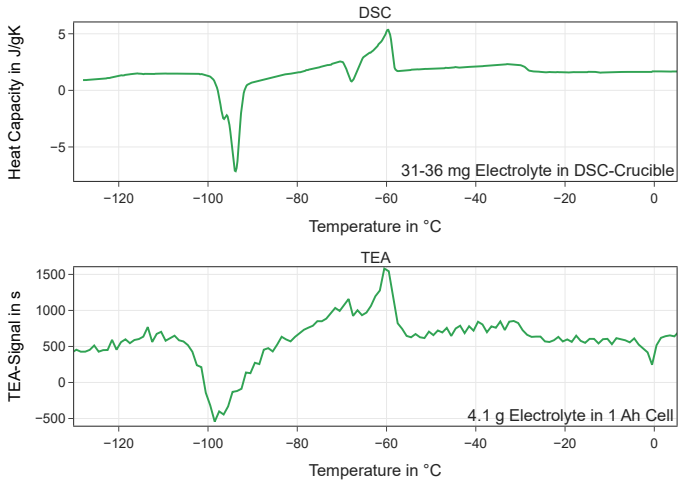

Fig. S2 Qualitative comparison of DSC and TEA measurements.

Quantifying Melting Behaviour of Electrolyte by DSC

The data for the quantitative and qualitative validation of the TEA were determined using a heat-flux DSC (Netzsch DSC 204, Germany). Sample preparation was carried out in an argon filled glovebox using concavus crucibles with a volume of 40 μl. The sample mass of the electrolyte was about 30 mg each. As the crystallisation of battery electrolytes is strongly dependent on crystallisation nuclei, according to Ding et al[52], two layers of the separator extracted from the cells used for the other experiments were placed on the bottom of the crucible before filling with the electrolyte. This was done to ensure a more comparable behaviour of the DSC experiment with respect to the measurement of the whole cell using TEA.

For the determination of the heat capacity data for the quantitative validation presented in Figure S4, the same calibration of the DSC, experimental setup and calculations were used as described in a precious publication[50]. The accuracy of the heat capacity measurement is about 5 %, according to Hoehne et al.[51]. Since the temperature of the experiment and heating rate in this work differ from the previous publication, the heating rate of the calibration was 1 K/min. The used calibration is described above.

For both the quantitative and qualitative validation, three samples each were measured with two cooling and two heating ramps, including isothermal sections of 20 min in between. The cooling rate was 10 K/min to have a high cooling rate according to the rapid cooling rate of the cell frozen using liquid nitrogen in the TEA. The heating rate was 1 K/min, which is in the same range of magnitude than the heating rate of the cell in the TEA experiment. Only the second heating ramp was used for the calculation. The data shown in Figure S4 is the mean value of the three samples. A description of processes occurring while the cooling and heating step are discussed together with the literature data of Ding et al[52] in the Supporting Information.

Validation of TEA

To validate the TEA we used a cell filled with electrolyte and compare the results qualitatively and quantitatively with the DSC-results obtained from electrolyte with the same composition.

To achieve a quantitative result, a calibration of the experimental setup is required. 2-propanol was used owing to its known melting enthalpy, a melting point in a similar range as the electrolyte, and its availability in the lab. The specific melting enthalpy of 2-propanol is 90.02 J/g according to[53]. Pouch cells containing four different amounts of 2-propanol (2.5,3,3.5, and 4 ml) were prepared using a pipette. The weight difference before and after filling was measured to calculate the inserted mass including losses due to evaporation of 2-propanol during vacuum sealing. Based on the actual mass the melting enthalpy can be calculated.

These melting enthalpies enable the calculation of R_{th} using a linear regression on the relationship of the area obtained from integrating the peak of the TEA-signal and subtracting the baseline, as shown in Figure S3. The zero crossing (Peak Area of 0 Ks and energy required for melting of 0 J) is used with a weight of 100 to calculate the linear regression due to the theoretically founded expectation that the peak vanishes if no liquid melts. The peak of the melting process is around the expected melting temperature ($-89\,^{\circ}$C). For lower amounts the peak rises slower resulting in a wider peak and a slightly higher peak temperature. We attribute this to reduced thermal conductivity of the cell with dry pores which occur due to insufficient 2-propanol to fill all pores. The slope of the linear regression provides the thermal resistivity of our setup and can be used to quantify TEA measurements.

For a quantitative comparison a cell was filled with 3.5 ml of electrolyte and weighed before filling and after sealing to control the mass of the electrolyte which is 4.097 g. We measured the TEA signal of the cell immediately after filling, to avoid side reactions from influencing the result. By dividing the baseline-corrected TEA-signal by the calculated R_th (70.2 K/W) and the weight of the electrolyte we can calculate the specific energy required to increase the temperature of the electrolyte. The baseline was measured using a dry cell. The heat flow measured using the DSC can also be converted to the same quantity by dividing it by the heat rate. The comparison is shown in the main part of this publication.

To test whether the TEA works as intended, we calibrated the TEA setup as described in the SI. With this calibration a quantitative comparison between DSC results and the TEA is possible, although we mainly focus on a qualitative interpretation of the

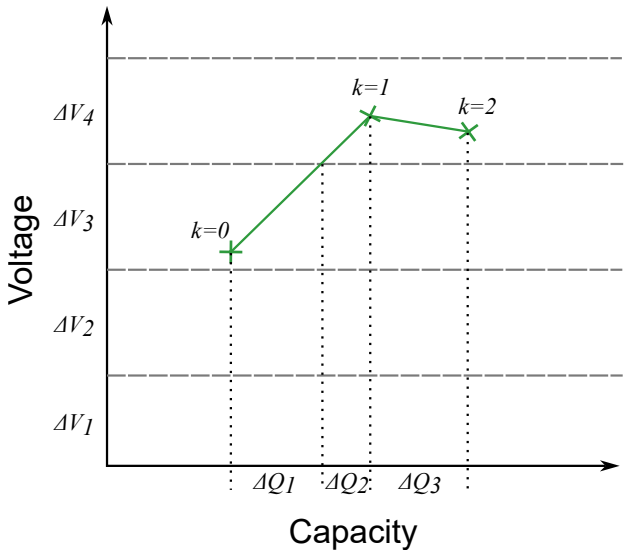

Fig. S5 Explanation of the adapted LEAN-Algorithm used in our work to calculate the ICA. Weights corresponding to ΔQ is used instead of a point-counter in the LEAN algorithm published in [25]

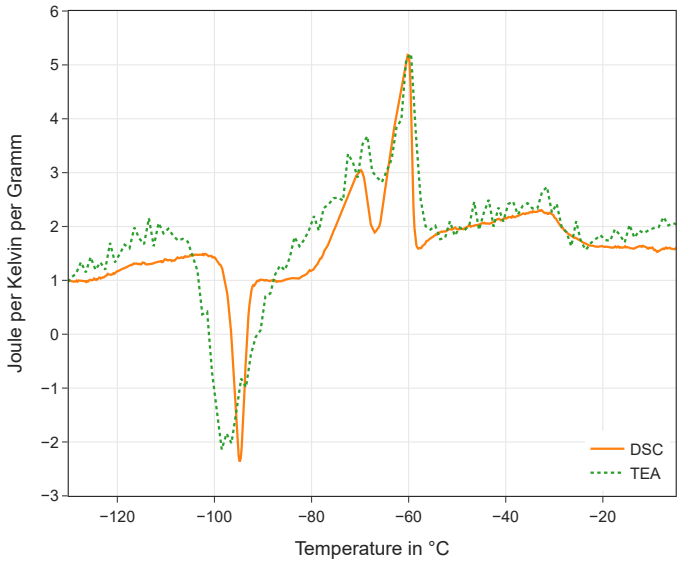

Fig. S4 Quantitative Comparison of DSC and TEA results. The signals match rather well given that the TEA 4.097 g electrolyte in a 1 Ah cell compared to the DSC where 27.7 mg of electrolyte is measured in a crucible.

melting points below. This comparison is shown in Figure S4. Qualitatively the two methods yield similar results despite testing very different amounts of electrolyte (27.7 mg in a crucible in case of the DSC and 4.097 g in a 1 Ah cell for the TEA). The exothermic peak is wider in case of the TEA compared to the DSC-measurement. Additionally, the first endothermic peak seems to be higher and wider for the TEA. The main endothermic peak at $-60\,^{\circ}$C matches rather well with the DSC-results. The same holds for the broad endothermic feature between $-55\,^{\circ}$C and $-30\,^{\circ}$C. At temperatures above $-20\,^{\circ}$C the TEA shows a rise of the heat capacity while the DSC remains constant.

The TEA presented here provides a simple setup which enables insights into the electrolyte which would otherwise require expensive equipment such as large calorimeters or cryostats. Compared to other methods used to elucidate the electrolyte such as GC-MS, no sample has to be taken from the cell and the cell is not damaged during TEA-measurements. However, the downside is the limited interpretability of the data due to limited availability of reference measurements yet.

Adapted LEAN-Method and qOCV-Fitting

The incremental capacity analysis was calculated using an adaptation of the algorithm described in [25]. This algorithm essentially assumes a quasi-monotonic function (which is a fair assumption for most OCVs) and equidistant sampling. Under these assumptions points within a small voltage window are counted to calculate the incremental capacity. Our adaptation is based on a linear interpolation between adjacent points on the capacity axis. Instead of counting the points a weight is added, which corresponds to the charge throughput in the respective voltage window. Figure S5 illustrates the process: ΔV_i represents the different voltage windows. The green line represents the voltage over capacity. The points for $k = 0$ and $k = 1$ are in different voltage windows (ΔV_3 and ΔV_4 respectively. Hence, a linear interpolation is used to calculate the weight added to the charge counter corresponding to ΔV_3 (ΔQ_1) and ΔV_4 (ΔQ_2), respectively. The next part (between $k = 1$ and $k = 2$) is within the same voltage window. Thus, ΔQ_3 is added to the charge counter corresponding to ΔV_4.

The ageing modes are analysed using half cell potential fitting. Half cell potentials are fitted to match the full cell. Four parameters are fitted as illustrated in Figure S6. The NMC622 used as a positive electrode can not be fully lithiated due to limited lithium diffusion as discussed in the main text. Thus, the starting point of the positive electrode potential does not refer to the fully lithiated state of the NMC622. This results in negative LLI values during the initial tests. During cycling, more and more lithium is lost which shifts the onset of the positive electrode potential curve to the left, eventually resulting in positive values for LLI.

Supplemental Coin Cell Measurements

To investigate the first cycle loss of NMC in more detail, coin cells with NMC622 as a positive electrode and metallic lithium as a negative electrode were assembled in a glove box under an inert argon atmosphere using the same electrolyte composition as used in this publication, EC:EMC 3:7 with 1M $LiPF_6$. One cell first discharged to 2.8 V after assembly and 1 h rest. It was then charged to an upper cutoff voltage which was increased for each cycle and discharged back to 2.8 V. The following upper cutoff voltages were used in this order 3.4, 3.6, 3.7, 3.8, 3.9, 4.0, 4.1, 4.2, and 4.35 V.

We identified a notable increase of the overpotential in the discharged state after charging the coin cell to 3.7 V. This coincides with the first major charge throughput in this partial cycle as shown in Figure S7. After this cycle, the relaxation remains very similar. Most importantly, no further increase of the overpotential is detected. In fact, the overvoltage seems to decrease slightly

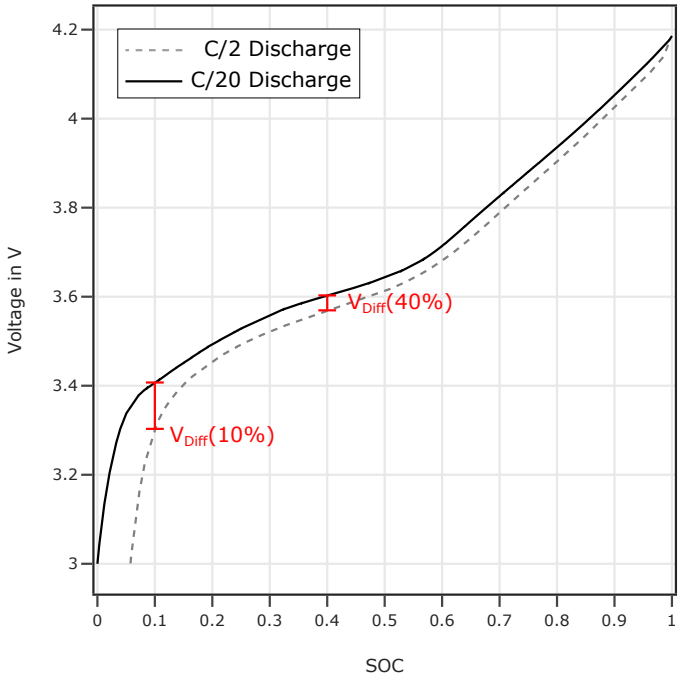

Fig. S8 Exemplary calculation of the SOC-dependent cycling resistance. The SOC is calculated based on the C/20 discharge. At specific points the voltage difference between this C/20 cycle and the corresponding point of the C/2 cycle is calculated. This voltage difference is then divided by the corresponding current difference to obtain the cycling resistance at this SOC.

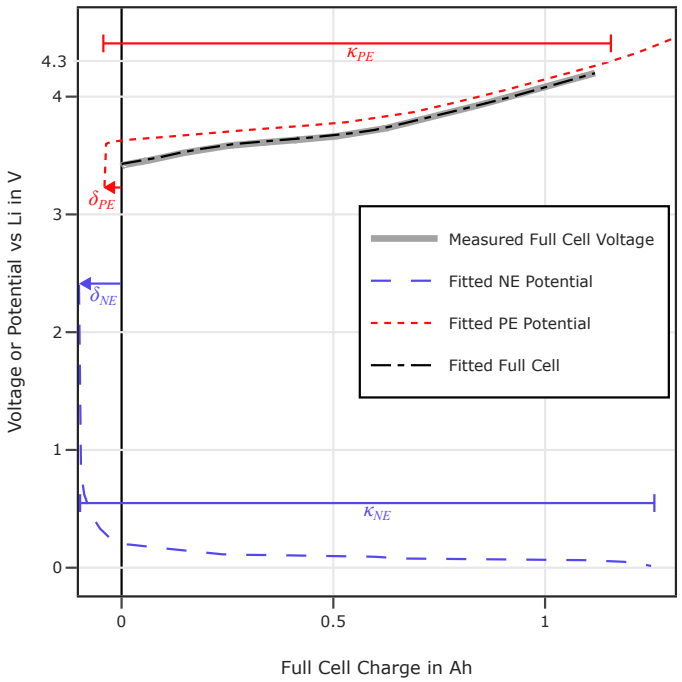

Fig. S6 Explanation of four parameters. δ indicated the shift on the charge axis relative to the discharged full cell, while κ indicates the capacity of the respective electrode.

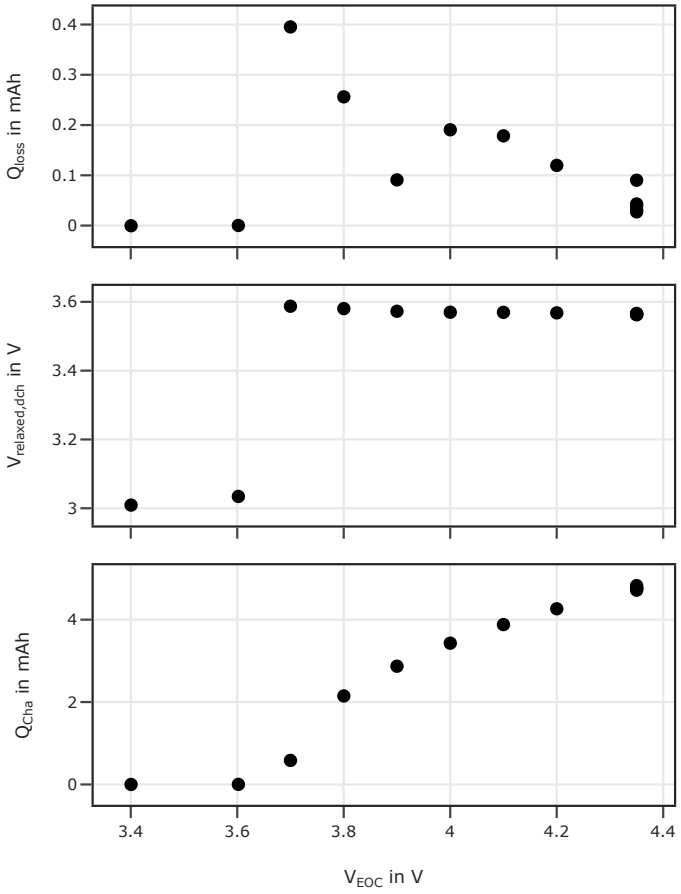

Fig. S7 Lost Charge (Q_{loss}), relaxed voltage after discharge ($V_{relaxed,dch}$), and the charged capacity (Q_{cha}) as a function of the end of charge voltage (V_{EOC}) of the charging process of aa NMC622|Li coin cell.

in each cycle. This indicates first a decrease of the lithiation followed by a slight increase in lithiation of the NMC at the end of discharge. The losses (defined as the difference between Q_{charge} and $Q_{discharge}$) are highest during the charge to 3.7 V and decrease in the subsequenct cycles where the cell is charged to 3.8 V and 3.9 V. At an end of charge voltage of 4 V the losses increase again. These losses cannot be attributed to a loss of lithium, as the lithium chip, used for the coin cell provides a huge surplus of lithium inventory.

Calculation of $R_{cycling}$

To calculate $R_{cycling}$ the Ah-counter during the RPT is normalised to the discharge capacity during the C/20 qOCV measurement. The charged cell at the beginning of this discharge has an SOC of 1 and the discharged cell has an SOC of 0. The difference between the voltage at a given SOC between the C/20 and C/2 tests can be calculated. Figure S8 illustrates this. Note that the SOC does not reach zero for the C/2 discharge due to the higher current.

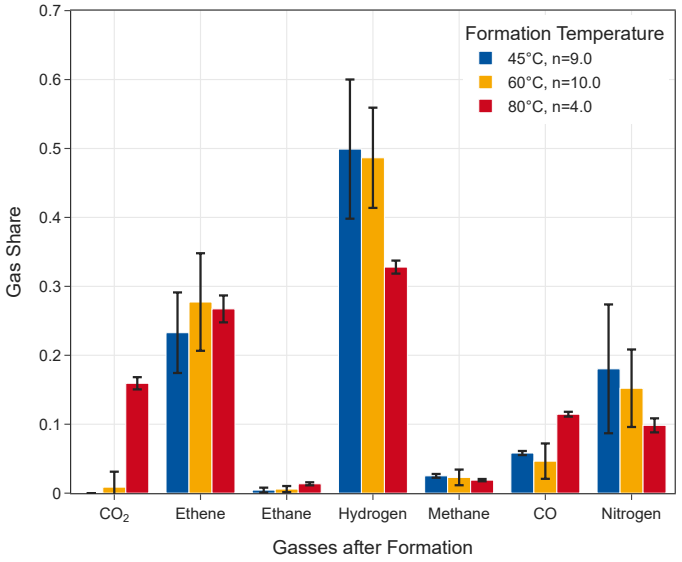

Fig. S9 Share of different gasses based on the samples analysed via GC. The bars represent the mean values of n measurements. The error bars indicate the standard deviation. The number of samples n is given in the legend.

Gas Quantification Procedure

The chromatograms are analysed using a custom Python script, which is described in detail here. Measurements of the calibration gas serve as a baseline. The composition of this gas-mixture is known and thus the amount of the different gas species can be calculated based on the injected volume. The assumption is that a linear relation between the peak area of the TCD-Signal and the amount of the corresponding gas species exists. The proportionality constant can be calculated based on the peaks obtained from the calibration measurement and the known volume of the corresponding gas species. The peak areas of the measurements of gas samples taken from cells can be assigned to the respective gas species by comparing the retention times. The peak area is then calculated by integrating the peak and subtracting a baseline using the same peak and baseline identification method as for the calibration gas. The proportionality constant is used to calculate the respective volume of the gas species in the sampled gas.

Quantification prior to Nitrogen-Normalisation

The gas composition for each formation temperature calculated based on the GC measurements is shown in Figure S9. Ethane and Methane are detected in all cells, regardless of formation temperature. Regarding the other quantified gasses, cells formed at 45 °C or 60 °C show a roughly similar gas composition: the major components are hydrogen and ethen, with nitrogen having the third highest share. Notably, only minor amounts of CO_2 are found in cells formed at 60 °C. At a formation temperature of 45 °C no CO_2 is detected.

Formation at 80 °C results in a considerably higher share of CO_2 and a higher share of CO. The share of ethene is in the same range as for lower formation temperatures. The shares of hydrogen and nitrogen are lower compared to the other formation temperatures.

Entropy coefficient

The effect of entropy on the charge throughput during formation is estimated based on the entropy coefficent of NMC622|Graphite cells reported in[30] and the measured incremental capacity at the end of charge. An entropy coefficient in the upper SOC range in the order of 5 $Jmol^{-1}K^{-1}$ in accordance with the measurements by Zhao et al.[30] is used for the estimation. To calculate the effect of the temperature on the open circuit potential, the entropy coefficent has to be divided by the faraday constant. The result is then multiplied by the temperature difference (20 °C) to obtain the voltage difference, which is roughly 1 mV. This represents the difference in the OCV induced by a temperature difference of 20 °C. Multiplying the change of OCV with the incremental capacity which is in the range of 1 Ah/V at the end of charge during formation, results in an additional capacity of cells formed at 60 °C of roughly 1 mAh compared to those formed at 80 °C. This is roughly a factor 10 below the observed difference.

Electrolyte Analysis using GC-MS

In addition to the results presented in the main part of this publication, cells were also investigated after the initial RPT to ensure the results did not merely reflect a transient state immediately after formation. Figure S10 shows the comparison between all measurements. The same components and dependency on formation temperature was found regardless of the time of sampling. Furthermore, the same components were present in the swab (sample taken from the edge of the cell) and the separator piece (taken from the center of the cell).

Charge Throughput and Initial Losses during Formation

The formation cycle is analysed by comparing the charge input during the charging phase of the formation cycle, the losses until the first full discharge to 3 V, and the ICA of the initial formation charging.

The charge input of the first charging cycle is highest for cells with a formation temperature of 60 °C as shown in Figure S11. It is similar for 45 °C and 80 °C. As the difference between the results is roughly in the range of the estimated errors, we calculated the p-value using a t-test. We consider the differences between 60 °C and the other two groups as significant under this test with $p = 0.015$. The lower charge input also translates to a slightly faster formation at 45 °C and 80 °C compared to 60 °C as the constant-current steps are the only steps that are not limited by time. To estimate the loss during the formation cycle, the charge balance from the beginning of the formation cycle (excluding the room-temperature wetting-period) until the end of the first full discharge of the cell was calculated and is displayed in Figure S11b. We refer to this as initial loss. This includes a contribution of lithium ions which remain in the graphite at the end of discharge. This initial loss is increasing with increasing formation temperature as shown in Figure S11. The results are statistically highly significant with $p < 3 \cdot 10^{-4}$ for all three combinations of the three groups. We will show below that the neglected amount

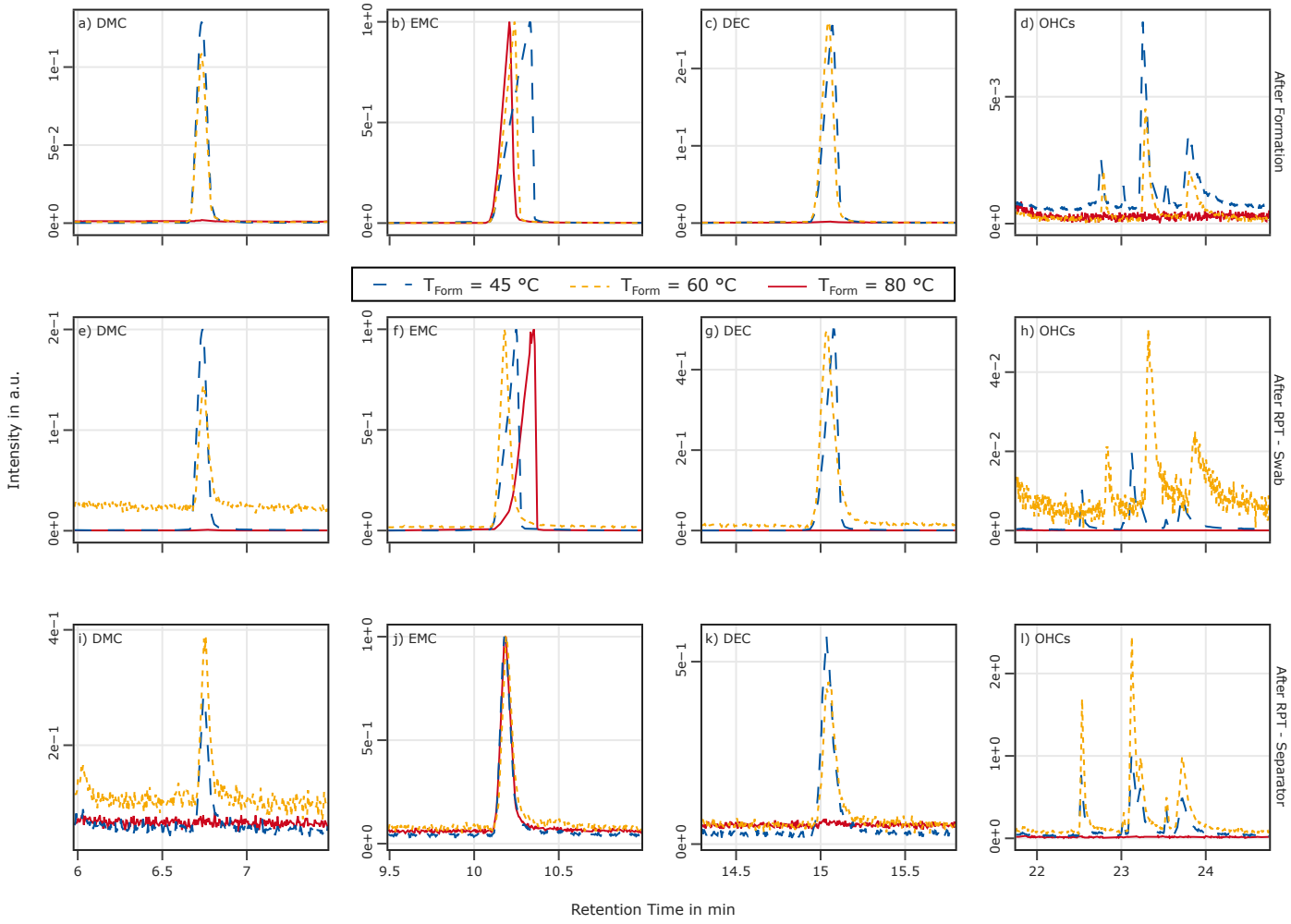

Fig. S10 GC–MS results of the electrolyte samples from the cells after formation (a–d) and after the RPT (e-l). The samples shown in Figures (e–h) were collected from the cell edge using a swab, whereas the samples corresponding to Figures (i–l) were obtained by taking pieces of the separator. The intensities were normalized to the intensity peak of EMC. Due to the large differences in signal intensities between the various components, the y-axis range is adjusted to the respective peak. Figures a), f) and k) show the intensities of DMC for all formation temperatures, b), g) and l) those of EMC, c), h) and m) those of DEC, and d), i) and n) those of EC. Figures e), j), and o) show the respective OHC signals.

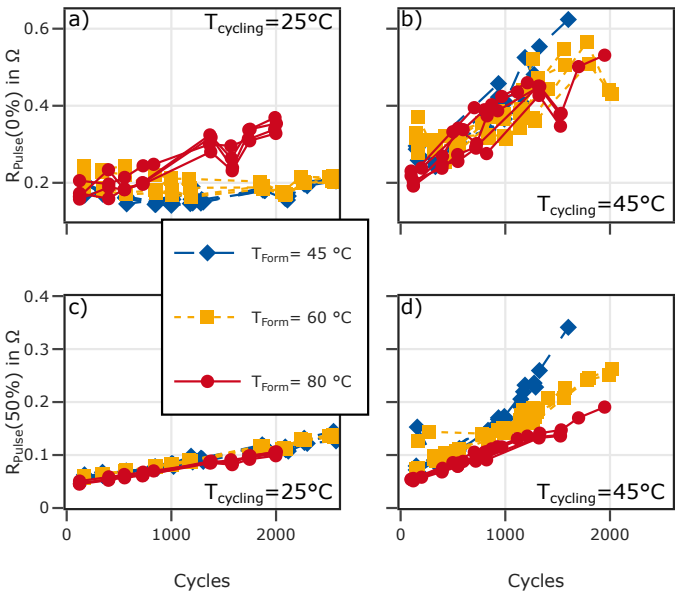

Fig. S12 Pulse resistance obtained from the C/2 discharge pulses during the RPT at 25 °C and 0% SOC (top) and 50% SOC (bottom). The left panels show the results from cells cycled at 25 °C. Results from cells cycled at 45 °C are shown on the right.

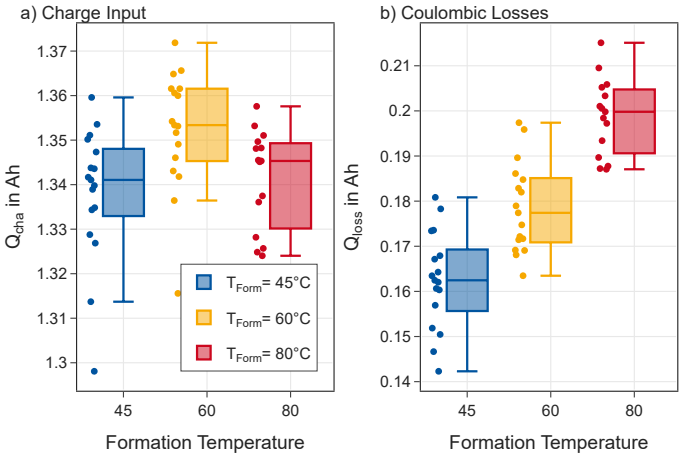

Fig. S11 Dependence between different formation temperatures and the charge input during formation (a), and the initial loss during the first formation cycle (b)

of lithium remaining in the graphite is higher at lower formation temperature, further exacerbating the difference observed here.

Discharge Pulse Resistance

Figure S12 displays the discharge pulse evolution at 0% and 50% SOC for cells aged at 25 °C and 45 °C.

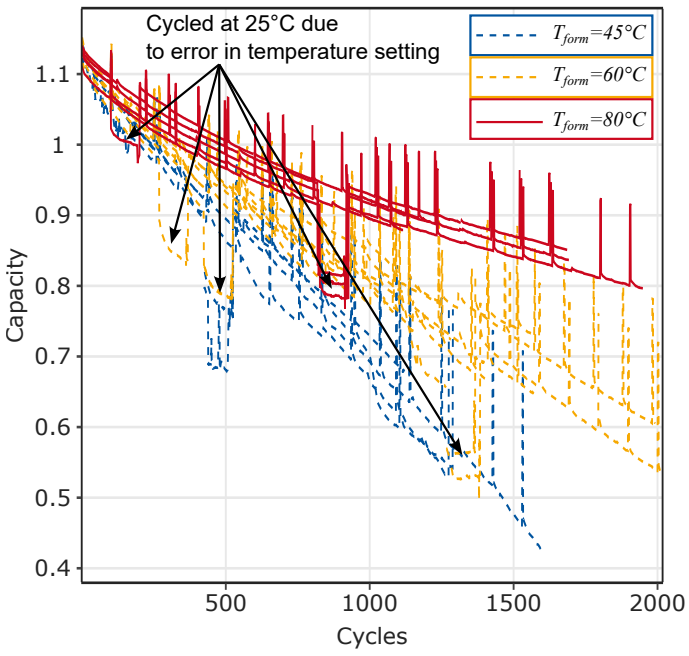

Fig. S13 Capacity during 1.5 C cycling at 45 °C. The same protocol as for cells cycled at 25 °C was used.

Ageing Tests at 45 °C

During the ageing test at 45 °C, the temperature adjustment after one RPT did not work properly resulting in cells performing some cycles at 25 °C. Once the error was noted, the tests were stopped for an additional RPT and afterwards continued with the correct cycling temperature of 45 °C. The lower temperature causes a capacity drop due to increased overvoltage. This is marked in Figure S13.

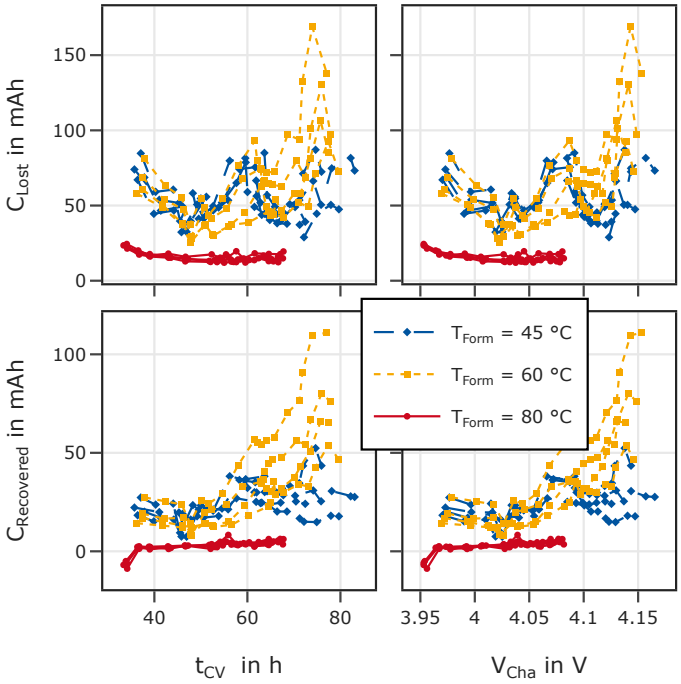

Fig. S15 Capacity lost during 100 fast charging cycles (top) and recovered capacity during three C/10 cycles (bottom) as a function of accumulated duration of the CV-phase t_{CV} (left) and the average charging voltage V_{Cha} (right) of the 100 cycles prior to the respective C/10 cycles. Only data from cyclic ageing at 25 °C has been evaluated here. Each line represents one cell. No consistent correlation of lost or recovered capacity with the CV duration or average charging voltage is found.

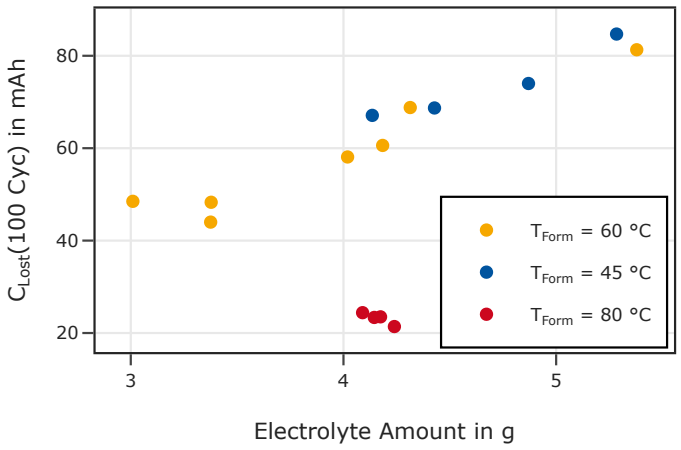

Fig. S14 The capacity loss observed during the first 100 cycles plotted with respect to the electrolyte mass measured as the difference of the cell weight before and after filling. Each point represents one cell. A linear correlation is observed for cells formed as 45 °C and 60 °C.

Additional cells with reduced electrolyte mass

In addition to cells with a minimum of 4 g of electrolyte, cells with lower electrolyte masses were assembled and underwent cyclic ageing. For the purpose of this paper, these cells were only used to add insights on the correlation between electrolyte mass and capacity fade during the first 100 cycles. A table detailing the electrolyte mass for each cell is supplied as part of the supplemental dataset.

The capacity loss observed during the first 100 cycles for cells cycled at 25 °C including those filled with less electrolyte are shown in Figure S14. Cells formed at 80 °C are included in this figure.

Correlation of CV-phase and Average Charging Voltage with Lost and Recovered Capacity

As discussed in the manuscript the overhang effect as dominant explaining factor would likely result in a strong correlation between the time the cells spend at high SOC and the capacity lost and recovered during the low current phases, respectively. Figure S15 shows that no such correlation, spanning all cells regardless of formation temperature exists.